communications physics

ARTICLE

https://doi.org/10.1038/s42005-023-01198-w OPEN

Remote focused encoding and decoding of electric fields through acoustoelectric heterodyning

Jean L. Rintoul [1], Esra Neufeld [2], Chris Butler [1], Robin O. Cleveland[3] & Nir Grossman [1]✉

Heterodyning of signals through physical multiplication is the building block of numerous modern technologies. Yet, it has been mostly limited to the interaction between electromagnetic fields. Here, we report that heterodyning occurs also between acoustic and electric fields in liquid electrolytes. We predict acoustoelectric heterodyning via computational field modelling, which accounts for the vector nature of the electrolytic acoustoelectric interaction. We then experimentally validate the spatiotemporal characteristics of the field emerging from the acoustoelectric heterodyning effect. The electric field distribution generated by the applied fields can be controlled by the propagating acoustic field and the orientation of the applied electric field, enabling the focusing of the resulting electric field at remote locations. Finally, we demonstrate detection of multi-frequency ionic currents at a distant focal location via signal demodulation using pressure waves in electrolytic liquids. As such, acoustoelectric heterodyning could open possibilities in non-invasive biomedical and bioelectronics applications.

[1] Department of Brain Sciences, Imperial College London, London, UK. [2] Foundation for Research on Information Technologies in Society (IT'IS), Zurich, Switzerland. [3] Institute of Biomedical Engineering, University of Oxford, Oxford, UK. ✉email: nirg@imperial.ac.uk

Heterodyning via physical multiplication of electrical or optical signals[1] in nonlinear devices such as diodes, transistors[2], photodetectors, or optical crystals is the building block of numerous scientific and technological applications ranging from radio and telecommunications[3,4], optical measurements[5], astronomical spectroscopy[6], chemical sensing[7], and quantum metrology[8]. Heterodyning provides a powerful means for frequency band shifting, optimizing signal transmission and spectral efficiency, and enabling accurate phase recovery of complex multifrequency signals[9]. Though existing heterodyning methods are ubiquitous, spanning solid-state semiconductors through to organic bioelectronics[10–12], they lack spatial focality and remote targeting. A method capable of remote, focal heterodyning in liquid materials would enable concepts such as liquid computation, or remote and focused momentary transistors to be developed.

In biomedicine, a long-standing goal has been to non-invasively and focally manipulate and record electrophysiological signals at depth. To date, this has been limited by the long wavelength of electric fields at the relevant frequencies, which exceeds anatomical length scales[13] (e.g., at 100 kHz, the wavelength in tissue is in the order of hundreds of metres), thereby preventing spatial interferential focusing (diffraction limit). Higher frequencies with wavelengths within the anatomical length scales (e.g., at 10 GHz, the wavelength in tissue is in the order of tens millimetres) have a low penetration depth in tissue. Remote focality has also been limited by the high dielectric heterogeneity of the tissue. For example, the cerebrospinal fluid in the brain leads currents away, preventing flexible targeting and precise focusing. In contrast to electric fields, acoustic fields have much shorter wavelengths at the same frequencies and a much better penetration, enabling spatial interferential focusing using established techniques such as beamforming at biological length scales[14]. In addition, the acoustic properties of tissues have smaller variability than dielectric properties. For example, in the brain, focusing is achievable if skull aberration can be corrected for[15]. Hence, it would be advantageous to harness acoustic waves' focusing ability for recording and manipulating electrophysiological signals.

Herein, we explore whether the electrolytic acoustoelectric phenomenon can be used for focal heterodyning of electric signals in conductive liquids. In the well-established solid-state piezoelectric effect[16], mechanical compression and rarefaction of non-centrosymmetric crystals modulate the material's electric dipole distribution. This electromechanical interaction generates an electric potential at the applied signal's frequency. The solid-state acoustoelectric phenomenon has underpinned numerous applications, including microphones, inkjet printers, and medical ultrasound imaging. In the less-established electrolytic acoustoelectric phenomenon, the mechanical compression and rarefaction modulate the ion density, thereby changing the spatial distribution of the conductivity[17]. According to Ohm's law[18], the mechanical modulation of conductivity perturbs the electric potential and the associated electric fields in the electrolytes. Recently, several studies have used this theoretical foundation and the lead-field reciprocal principle to estimate the current density distribution in tissues using ultrasound and surface electric potential recording aka ultrasound current source density imaging[19–22].

In this work, we unveil the properties of this fundamental interaction between acoustic and electric fields. We first develop a mathematical model describing the physics of the electrochemical interaction and then use the model and experimental measurements in physiological saline to investigate its spatiotemporal properties. We show that by applying a focal acoustic field to an electric field in electrolytes, we can mechanically heterodyne the electric field, inducing components that oscillate at the fields' sum and difference frequencies. The heterodyned electric field has a unique shape dependent on the relative applied fields' orientation enabling the encoding of electric fields at depth. Finally, we demonstrate that we can accurately decode a focally heterodyned signal by remotely demodulating an electric field, accurately recovering the original electric signal. These unique properties of the electromechanical interaction open translational avenues in electrochemistry, bioelectronics, and medicine.

Results

Mathematical model of acoustoelectric field generation in electrolytic liquids. Hitherto model of the electrolytic acoustoelectric phenomenon[23–25] has been based on Ohm's law which does not account for the vectorial and spatially dependent nature of the underlining physics. Thus, we developed a mathematical model of the phenomenon that captures these key characteristics using Gauss theory[26].

We assumed an external electric field $\vec{E}_o(x,y,z)$ that induces an ionic current with a density $\vec{J}(x,y,z)$ in a weak electrolytic liquid with a conductivity $\sigma(x, y, z)$. According to Gauss's law, the integral of the normal component of current vectors over a closed surface is equal to the integral of the current source density within the enclosed volume[26]. Thus, if we assume a current source that is external to the volume of interest, the divergence of the current density is zero at any location within the volume of interest.

$$\nabla \cdot \vec{J} = 0 \tag{1}$$

According to Ohm's law, the current density is equal to the product of the electric field and the conductivity[26].

$$\vec{J} = \sigma \vec{E}_o \tag{2}$$

Combining Eqs. (1) and (2) states that the divergence of the product of the ion conductivity and electric field is zero within the volume of interest.

$$\nabla \cdot (\sigma \vec{E}_o) = 0 \tag{3}$$

If a pressure field $P(x, y, z)$ is concurrently applied to the electrolytic medium, it changes the ion concentration and mobility resulting in a conductivity modulation $\sigma_{ae}(x, y, z)$. This conductivity modulation creates an electric field modulation $\vec{E}_{ae}$ such that Gauss's law of net-zero flux is satisfied. Thus Eq. (3) becomes

$$\nabla \cdot ((\sigma + \sigma_{ae})(\vec{E}_o + \vec{E}_{ae})) = 0 \tag{4}$$

Using Eq. (3) and neglecting higher order terms, Eq. (4) can be approximated as (see Supplementary Note 1 for full the derivation)

$$\nabla \cdot (\sigma \vec{E}_{ae}) + \nabla \cdot (\sigma_{ae} \vec{E}_o) = 0 \tag{5}$$

Earlier studies established that the relative change in conductivity is proportional to the applied pressure[27,28]

$$\frac{\sigma_{ae}}{\sigma} = kP \tag{6}$$

where k is a constant incorporating the pressure-induced changes in the relative molar concentration and ionic mobility (see Supplementary Note 1 for more details). Combining Eqs. (5) and (6) gives

$$\nabla \cdot (\sigma \vec{E}_{ae}) = -\nabla(kP) \cdot (\sigma \vec{E}_0) \tag{7}$$

If the electrolytic medium and the baseline electric field are homogenous, Eq. (7) can be written as

$$\nabla \cdot \vec{E}_{ae} = -k\overrightarrow{\nabla P} \cdot \vec{E}_{o} \quad (8)$$

where $\overrightarrow{\nabla P}$ is the gradient of the acoustic field. Equation (8) is the governing equation of the mathematical model describing the acoustoelectric phenomenon in a homogenous electrolytic medium. The left side of the equation is similar to Maxwell's first equation[26], implying that the acoustoelectric interaction phenomenologically results in the generation of an electric field source proportional to the dot product of the acoustic field gradient and the electric field. The multiplication of the acoustic and electric fields in the equation predicts that the generated electric field oscillates at the mixing product frequencies, i.e., the sum and difference of the original fields' frequencies.

In the case of an ideal planar and infinite transducer that can be modelled one-dimensionally and an electric field aligned with that direction, Eq. (8) can be simplified to (see Supplementary Note 1 for full derivation)

$$\vec{E}_{ae} = -kP\vec{E}_{o} \quad (9)$$

In this special case, the governing equation of the acoustoelectric effect is reduced to the previously derived scalar description of the effect[25] in which the pressure gradient and the orientation between the acoustic and electric fields can be ignored.

Computational investigation of the acoustoelectric effect. Next, we used electromagnetic and acoustic simulations to explore the spatiotemporal properties of the acoustoelectrically generated field in physiological saline solution, as saline closely mimics both acoustic and electromagnetic tissue properties[29,30]. We applied a continuous focal acoustic field and a homogenous electric field at various frequencies and amplitudes (see Supplementary Note 2 for the characterization of applied and generated fields). We modelled the transducer's acoustic fields analytically, using a summation of Bessel functions[31] (see Supplementary Fig. 2a, b for spatial maps of the acoustic field amplitude and amplitude gradient. Based on previous experimental studies[23,28,32]), we set the constant k to $1e^{-9}\,Pa^{-1}$. To estimate the acoustoelectrically generated electric field, we computed Eq. (8) for the induced electric potential ϕ_{ae}, with $\vec{E}_{ae} = -\nabla\phi_{ae}$, with a fast Poisson solver that operates in the Fourier-space (i.e., k-space); see the "Methods" section for more details on the computation procedure.

We found that when the electric field was applied in parallel with the direction of the acoustic field propagation (Fig. 1a), the generated electric field had a three-dimensional topology with a concentric ring dipole in the radial direction (Fig. 1b) and a periodic linear multipole in the axial direction (relative to the acoustic field propagation) with the ultrasound wavelength (Fig. 1c). The amplitude of the generated electric field was proportional to the amplitudes of the applied acoustic field and electric field (Supplementary Figure 2d). For example, the application of an acoustic field with a peak amplitude of 1 MPa via a spherical 500 kHz transducer (63.2 mm radius of curvature, ROC) and an electric field with an amplitude of ~3 kV/m, generated an electric field of ~0.17 V/m, corresponding to an acoustoelectric field's coupling factor c_{ae} of ~55 pPa^{-1} (pPa^{-1}, pico-pascal^{-1}), where c_{ae} is the ratio between the peak amplitude of the acoustoelectrically generated electric field and the product of the applied electric field and peak acoustic field.

When the electric field was applied perpendicular to the direction of acoustic field propagation (Fig. 1d), it changed the topology and strength of the generated electric field. Specifically, the concentric ring geometry in the radial direction changed to a dipole (Fig. 1e, see also Fig. 2a for an amplitude distribution comparison). The amplitude of the generated field decreased as the acoustic propagation direction and electric fields' alignment dropped (Fig. 2b). We found that the generated electric field was about four times larger when the applied fields were in parallel as compared to perpendicular.

When a DC electric field was applied, the polarity of the generated electric field changed periodically at the acoustic frequency (Fig. 2c). However, if the electric field was applied at a frequency different from the acoustic frequency, the generated electric field changed periodically with components at the difference and sum frequencies of the electric and acoustic fields (Supplementary Fig. 2c). The instantaneous amplitude of the generated electric field was maximal/minimal when its components at the sum and difference frequencies were superimposed constructively/destructively. Thus the maximum amplitude of the sum and difference frequency envelope was twice that of the single frequency when a DC field is applied, i.e. c_{ae} was 110 pPa^{-1}.

Applying ultrasonic fields at higher frequencies reduced the diameter of the generated electric field focus due to the smaller pressure foci (Fig. 2d, e). The smaller acoustic foci resulted in a generation of a stronger electric field due to the higher acoustic field gradients (Fig. 2f, g). For example, c_{ae} was 55 pPa^{-1} with a 500 kHz acoustic frequency and 2000 pPa^{-1} with a 4 MHz acoustic frequency, while peak pressures remained constant at 1 MPa.

Validation of the acoustoelectric effect in physiological saline. To experimentally verify frequency mixing and predicted spatial properties of the acoustoelectric phenomenon we conducted experiments with an ultrasound source and an electric field in physiological saline. A 500 kHz focused ultrasound transducer (ROC = 63.2 mm) was used to create the acoustic field, and a pair of Platinum Iridium electrodes (0.25 mm diameter, 3 mm spacing) were used to create the constant electric field which was moved around with the measurement electrode. The acoustoelectrically generated field was measured by a third electrode (0.25 mm diameter) relative to a remote reference electrode (see Fig. 3a–c for a schematic representation of the experimental setup). The saline had a conductivity of 1.6 S/m similar to biological tissues[33]. See the "Methods" section for more details, Supplementary Note 3 for characterization of the applied electric and acoustic fields and Supplementary Note 4 for instrumentation details.

We first applied an electric field ($f_E = 8$ kHz) parallel to the acoustic field ($f_A = 500$ kHz) propagation direction and measured the electric fields at the acoustic field focus. We found that the combined fields generated electric field components oscillating at the difference and sum frequencies, i.e., $\Delta f = 492$ kHz and $\sum f = 508$ kHz (Fig. 3d–f), as was predicted by our mathematical model (Eq. 8). The onset of the measured electric field corresponded to the arrival of the acoustic field in the electric field region (Supplementary Fig. 4a). There were no electric field oscillations at the difference and sum frequencies when the acoustic field or the electric field were applied individually (see Supplementary Fig. 4b,e for statistical analyses and representative time series traces).

We then applied the electric field, sweeping through a broad range of frequencies between 10 kHz and 500 kHz while keeping the acoustic frequency fixed at 500 kHz. We found a consistent generation of electric field components at the difference and sum frequencies across the applied frequencies range (Supplementary

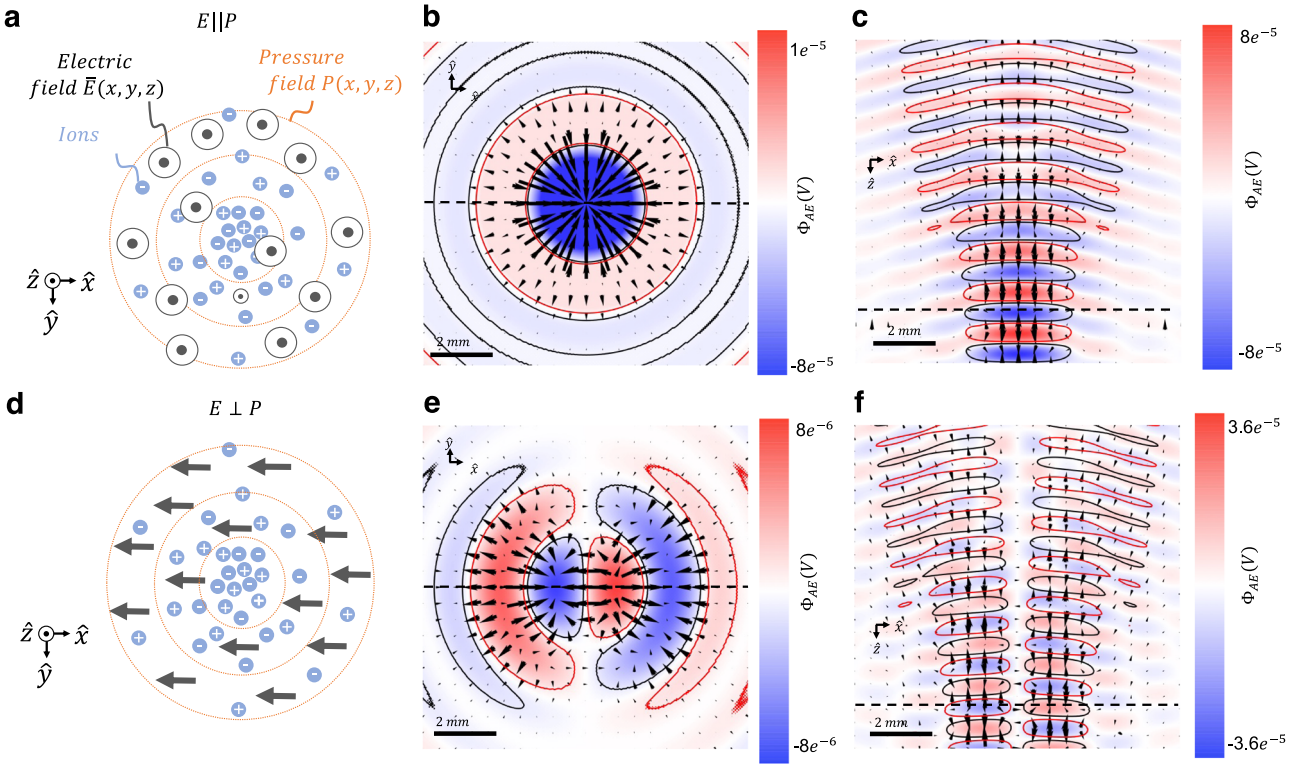


Fig. 1 Computation of the acoustoelectric effect in weak electrolytes. Characteristics of the electric field $\vec{E}_{AE}$ generated by focal acoustic field $P(x, y, z)$, here $f_A = 500$ kHz and peak amplitude 1 MPa, and homogenous electric field $\vec{E}(x, y, z)$ here $f_E = 0$ Hz (i.e., DC) and amplitude 3.2 kV/m. **a** Schematic of the computational model in which $\vec{E}$ is applied in parallel to the propagation direction of the acoustic field P. **b** Spatial distribution of the acoustoelectrically generated electric field in the focal plane of the ultrasound. Radial plane $\hat{x}\hat{y}$ distribution along the black dashed line in **c**; shown are $\vec{E}_{AE}$ vector lines (arrows) and the corresponding electric potential Φ_{AE} maps (colour scale, with contour lines indicating equipotential). **c** Axial plane $\hat{x}\hat{z}$ distribution, showing the same as (**b**) but note the different scale. **d** Same as (**a**) but with $\vec{E}$ perpendicular to the propagation direction of P. **e**, **f** Same as **b** and **c** but with $\vec{E}$ perpendicular to the propagation direction of P.

Figure 4c). We found the timescale of temperature change due to acoustic energy deposition was outside the range of the acousto-electric potential variation (Supplementary Fig. 4f, g). The acoustoelectric coupling factor c_{ae} decreased as the liquid temperature increased (Supplementary Fig. 4h), indicating the temperature of the electrolytic liquid plays a role in the amplitude of the generated fields. Figure 3g–i show representative fields' traces when the frequency of the applied electric field differs from the acoustic frequency by only a small amount ($f_E = 499.99$ kHz, $f_A = 500$ kHz; $\Delta f = 10$ Hz, $\sum f = 999.99$ kHz), generating an electric field that oscillates at a low frequency within the electrophysiological spectrum[34,35], whilst the applied high-frequency field is outside the electrophysiological relevant range[36], showing how electric fields can be encoded at depth.

After confirming that the electrolytic acoustoelectric effect multiplies the acoustic and electric fields yielding an electric field with components that oscillate at the fields' sum and difference frequencies, we explored the spatiotemporal characteristics of the generated electric field by repeating the electric field measurements across the acoustic field region to build a time-synced two-dimensional distribution. We found that when we applied the electric field parallel with the direction of the acoustic field propagation (as in Fig. 1a), the generated electric field had a concentric ring dipole in the radial direction (Fig. 4a) and a periodic linear multipole in the axial direction (Fig. 4b), as was predicted by our computational modelling (see Fig. 1b). Shaping the topology of an electric field with an acoustic field, is potentially a way to create an electrostatic lens[37,38].

When we applied the electric field perpendicular to the direction of acoustic field propagation (as in Fig. 1d), the concentric ring geometry in the radial direction changed to a linear dipole (Fig. 4c, d), revealing, an orientation-dependent field distribution as was predicted in our computational modelling (see Fig. 1b–f). Figure 4e shows a comparison of the normalized field amplitude profile along a radial axis (see Fig. 2a for corresponding computation). The ratio between peak amplitudes when comparing the parallel and the perpendicular orientation was 4.12 ± 0.36 (mean ± st.d.; $n = 50$ measurements; Fig. 4f), as was predicted by our computational modelling (see Fig. 2b). The generated electric field distribution was a superposition of the components oscillating at the sum and difference frequencies, resulting in an envelope minimum (as measured at the local waveform maxima) when the two sine wave components were in an antiphase relationship and a maximum when they were in phase (Fig. 4g). This reveals the amplitude of the acoustoelectric interaction is dependent on this frequency mixing time evolution.

The amplitude of the generated electric field was proportional to the applied acoustic and electric fields (Supplementary Fig. 4d). When the acoustic field was applied with a peak amplitude of 1 MPa, the ratio between the generated and applied electric fields was 1–250 when the maximal value was taken across the 0.1 s recording span, corresponding to an acoustoelectric field coupling factor c_{ae} of ~2000 pPa^{-1}, i.e., larger than the simulation prediction of 110 pPa^{-1}. For example, an application of an acoustic field with a peak amplitude of 1 MPa and an electric field with an amplitude of 250 V/m generated an electric field that oscillates at the sum and difference frequencies with a peak

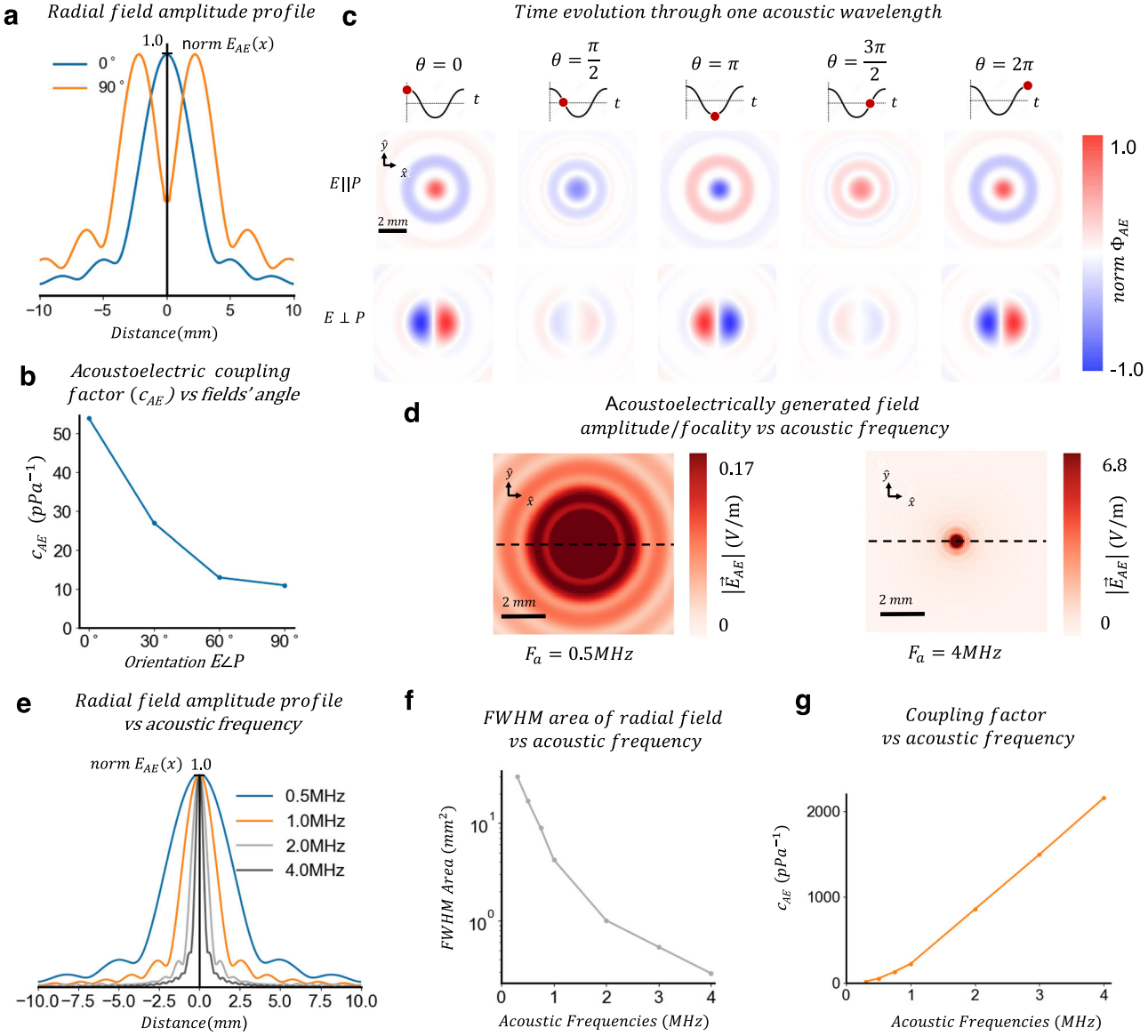


Fig. 2 Simulation predictions of the acoustoelectric effect in weak electrolytes. a Line plot comparing the normalized amplitude of generated field $|\vec{E}_{ae}|$ along the black dashed lines in Fig. 1(b) and (e). **b** Acoustoelectric coupling factor c_{ae} vs. angle between the applied electric field and acoustic propagation direction. **c** Evolution of the generated electric field over time shown at the same point in space (focus) as time progresses over an acoustic wavelength. Shown are Φ_{AE} maps in the radial plane $\hat{x}\hat{y}$ at different phases of the ultrasound transducer period for a parallel and perpendicular electric field orientation; θ, instantaneous phase of the applied acoustic field. **d** Effect of the applied acoustic field frequency on the generated electric field. Electric and acoustic fields were applied as in Fig. 1a but at different acoustic frequencies. Representative $|\vec{E}_{AE}|$ maps in the radial plane $\hat{x}\hat{y}$ with acoustic field at $f_A = 500$ kHz and $f_A = 4$ MHz, respectively. **e**, Normalized $|\vec{E}_{AE}|$ along the $\hat{x}$ direction vs. applied acoustic frequency. **f** Full-width half maximum (FWHM) area of the generated field vs. applied acoustic frequency decreases as frequency increases. **g** Acoustoelectric coupling factor vs. applied acoustic frequency increases as frequency increases.

amplitude of 1 V/m. The higher coupling factor might be attributed to a larger change in the ionic mobility, which would affect the constant k since the adiabatic compressibility at 20 °C in water is well established at 1 MPa to be 4.6e−10 Pa^{-1}[39], and all the other parts of the equation are experimentally verified.

Remote, focal heterodyning and demodulation of electric signals. After confirming that the electrolytic acoustoelectric effect multiplies the acoustic and electric fields, we explored whether this principle could be utilized to remotely and focally heterodyne electric signals in liquid electrolytes and detect them without losing information, similar to how amplitude-modulated (AM) radio transmission operates[40]. Shifting a low-frequency electric signal to a higher one, provides powerful signal-to-noise advantages in noisy environments such as the body, as signals at focal spatial locations of interest can be isolated via frequency modulation[41]. We applied a complex electric signal (consisting of a superposition of 8, 9, and 11 kHz sine waves) to the acoustic field focus and recorded the acoustoelectrically generated electric potentials as before. To recover the original signal from the generated higher frequency potential, we deployed an in-phase and quadrature (IQ) demodulation strategy[42,43]. See Fig. 5a for a schematic of the acoustoelectric heterodyning and demodulation procedure. Figure 5b–d shows representative traces of the input ionic current signal, the acoustoelectric heterodyned signal, and the recovered demodulated signal, with Fig. 5e–g showing their

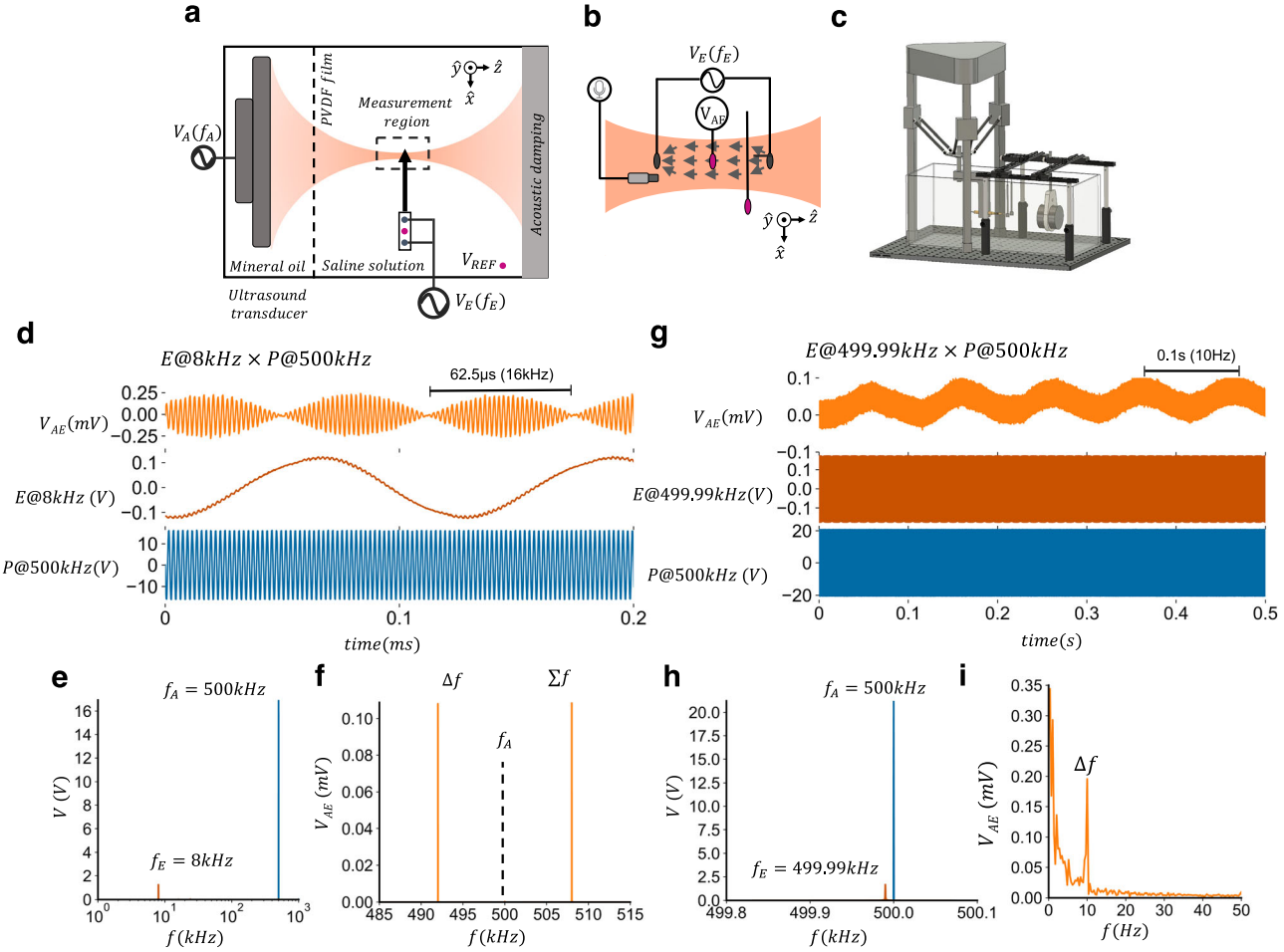


Fig. 3 Measurements of acoustoelectric frequency mixing in a tissue phantom. Time-frequency characteristics of the electric field generated by simultaneous application of a focal acoustic pressure field $P(x,y,z)$ and an electric field $\vec{E}(x,y,z)$ to a saline filled tank. **a** Schematic of the experimental setup, showing setup overview, **b** zoomed view of the boxed measurement region in (**a**); V_A applied electrical potential from RF power amplifier driving the ultrasound transducer at a frequency f_A; V_E, applied electrical potential from arbitrary waveform generator and custom-made voltage source to the electrodes at a frequency f_E; V_{AE} measured acoustoelectrically generated electric potential (see Supplementary Figs. 3, 4 for characterization of the experimental setup). **c** Sketch of experimental apparatus. **d** Representative recordings when the electric field is applied at a frequency $f_E = 8$ kHz and the acoustic field at a frequency $f_A = 500$ kHz. Shown are traces of applied acoustic field P (blue), applied electric field V_E (red), and generated electric potential V_{AE} (orange); V_{AE} was filtered before logging (high-pass filter, cut-off frequency 100 kHz). The superposition of the sum frequency ($\sum f = 508$ kHz) and difference frequency ($\Delta f = 492$ kHz) is manifested in V_{AE} as a periodic modulation of the envelope amplitude at their difference frequency $\sum f - \Delta f = 16$ kHz. **e** Amplitude spectral density (ASD) of the signal traces in (**d**) showing the applied V_A and V_E traces, **f** ASD of recorded V_{AE} trace with peaks at the frequency mixing products Δf and $\sum f$ but not at the acoustic frequency f_A. **g**, (**i**) Same as (**d**) but for an electric field at $f_E = 499.99$ kHz (i.e., $f_E \approx f_A$). V_{AE} was filtered before logging (low-pass, cut-off frequency 5 kHz) to remove the high-frequency electric field, which also removes the sum frequency. An oscillation at the difference frequency $\Delta f = f_A - f_E = 10$ Hz is evident. **h** Amplitude spectral density (ASD) of the signal traces in showing the applied V_A and V_E traces, **i** ASD computed from V_{AE} trace in (**g**).

respective spectral components. We found that the original electric signals can be accurately recovered from the acoustoelectrically generated electric fields (Fig. 5h). The cross-correlation between the recovered and input signals was 0.87 ± 0.063 (mean ±std; $n = 10$ measurements).

Discussion

In this work, we show evidence that the electrolytic acoustoelectric phenomenon involves frequency mixing such that the sum and difference frequencies are created in the resultant electric field. The resultant electric field has a unique spatial distribution that depends on the relative fields' orientation, varying from periodic concentric rings to a dipole source. We demonstrate how these unique properties can be utilized to encode and decode complex electric signals remotely and focally.

Earlier studies of the phenomenon have helped to understand the acoustoelectric coupling factor[27,28] and started to explore applications such as current source density imaging[20–22]. Our work builds on these original studies to further advance the understanding of the phenomenon by unveiling its frequency mixing property and complex field-dependent shape. In addition, we present a theoretical model capturing the vectorial nature of the underpinning physics and show that the hitherto theory is a special, one-dimensional case with paraxial acoustic propagation. These findings provide a conceptual framework to design, interpret, and translate the electrolytic acoustoelectric phenomenon.

We found a higher acoustoelectric coupling factor than has been previously reported, potentially due to a larger change in the ionic mobility, given the well-established adiabatic compressibility of water ($4.6e{-}10\ \mathrm{Pa}^{-1}$ at 20 °C)[39]. For the experimental results to match the simulation, the constant k would need to be $2e^{-8}\ \mathrm{Pa}^{-1}$,

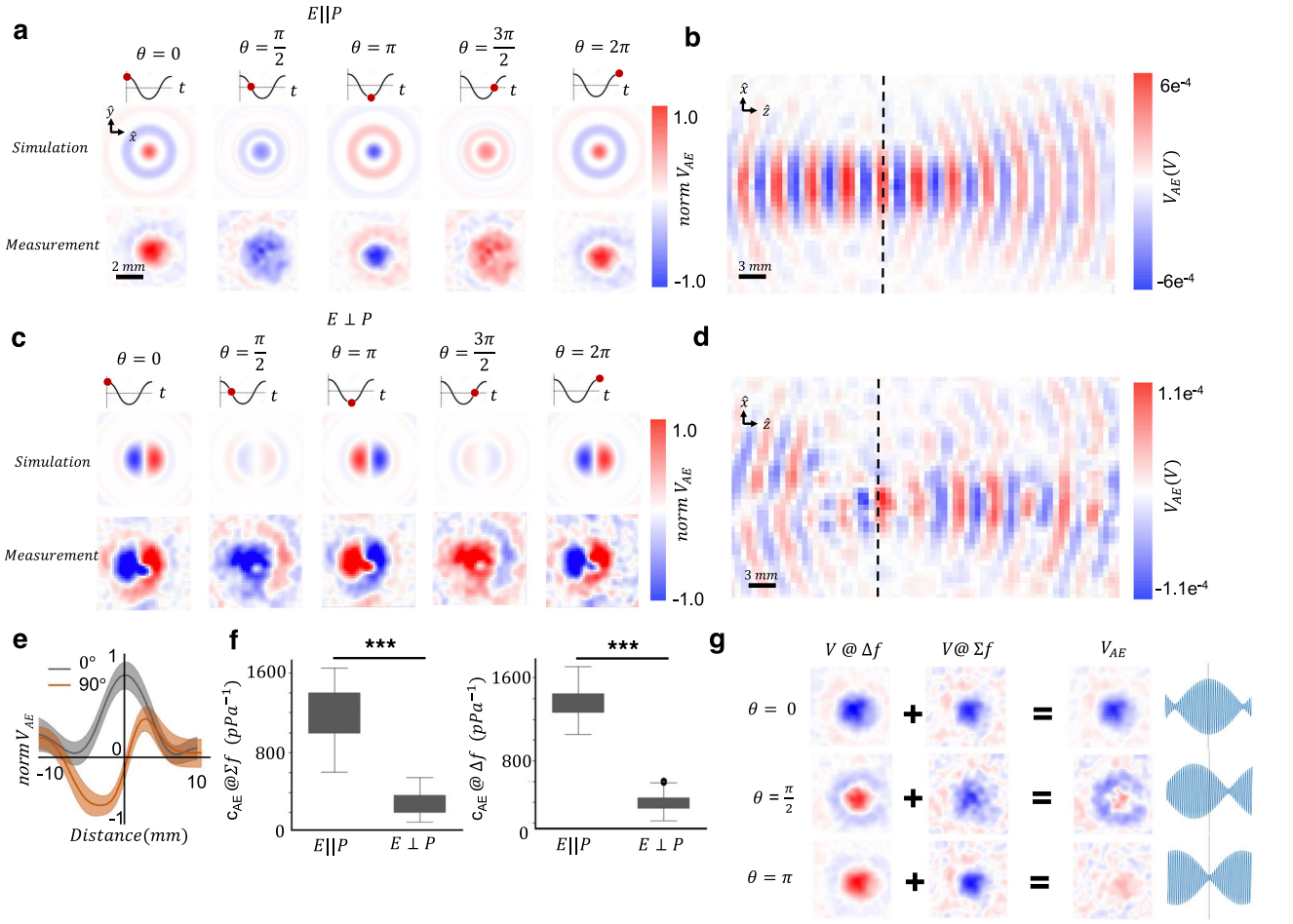


Fig. 4 Measurements of acoustoelectric fields' spatiotemporal characteristics in a physiological phantom. Spatiotemporal characteristics of the electric field generated by simultaneous application of a focal acoustic pressure field $P(x,y,z)$ at a frequency $f_A = 500$ kHz propagating in the $\hat{z}$ direction and an electric field $\vec{E}(x,y,z)$ at a frequency $f_E = 8$ kHz. Measurement setup same as in Fig. 3a, but with the measurement probe scanned across the volume. **a** and **b** The applied electric field is parallel to the propagation direction $\hat{z}$ of the applied acoustic field. **a** Spatial distribution of the measured electric potential V_{AE} (normalized to max value) in the radial plane $\hat{x}\hat{y}$ at the black dashed line in (**b**) shown at different phases θ of the acoustic period ($1/f_A$), together with the simulated distribution (as in Fig. 2b). **b** Spatial distribution of the measured electric potential V_{AE} in the axial plane $\hat{x}\hat{z}$. **c** and **d** The applied electric field is perpendicular to the propagation direction $\hat{z}$ of the applied acoustic field, shown are as in (**a**) and (**b**). **e** Line plot comparing the measured electric potential V_{AE} normalized to max value along the black dashed lines in (**b**) and (**d**). **f** Acoustoelectric coupling factor at the sum frequency $\sum f$, and the difference frequency Δf, shown values are mean ± st.d.; *** indicates $p < 10e^{-20}$; significance was assessed using paired t-test; $n = 50$ measurements. **g** Spatial distribution of the measured electric potential V_{AE} at the difference frequency Δf and sum frequency $\sum f$ and their superposition (normalized to max value) in the radial plane $\hat{x}\hat{y}$ at different phases θ of the acoustic period ($1/f_A$).

necessitating the ionic mobility contribution to be ~20 times larger than the contribution due to adiabatic compressibility.

Given the broad use of electrostatic focusing lenses to focus electron beams with electric and magnetic fields[37,38,44], the potential translational prospects for acoustically controlled electric field lenses are exciting. The acoustoelectric heterodyning could enable non-invasive focal modulation and recording of electrophysiological signals at depth. For example, remote, focal modulation of neural activities could be achieved by generating electric fields with a difference frequency Δf within the physiological range (<100 Hz) while keeping the frequency of the applied electric fields f_E sufficiently high (>1 kHz) so it is attenuated by the low pass filtering of the cell membrane[45]. However, the low efficiency of the acoustoelectric conversion may render such focal neural modulation challenging. For example, generating an electric field of 1 V/m (a typical neuromodulation threshold[46]) at Δf may require applying an electric field of hundreds V/m and an acoustic field of hundreds kPa that might be themselves strong enough to affect neural activity. Future studies in animal models will be able to test the feasibility of such an approach. Remote, focal recording of neural activities could be achieved by applying a focal acoustic field to the target region to up-convert the endogenous neural signals to a higher frequency range (i.e., the sum and difference frequencies of the acoustic field), thereby rendering them electrically detectable remotely. Furthermore, the large spatial gradient of the acoustoelectrically generated electric fields may intensify focal ultrasound neuromodulatory applications[47] and enable strong dielectrophoresis forces with the potential to suppress tumour cell mitosis[48].

In summary, we show how the spatial precision of ultrasound can enable focal heterodyning of electric fields. Given the ubiquitous use of signal heterodyning in solid-state electronics, these findings could open frontiers in remote electrochemical, bioelectronics and medicine, with the potential for developing devices that are less invasive or completely non-invasive.

Methods

Computational modelling of the acoustoelectric fields. The computations of the acoustoelectric modulation of the applied electric and acoustic fields were

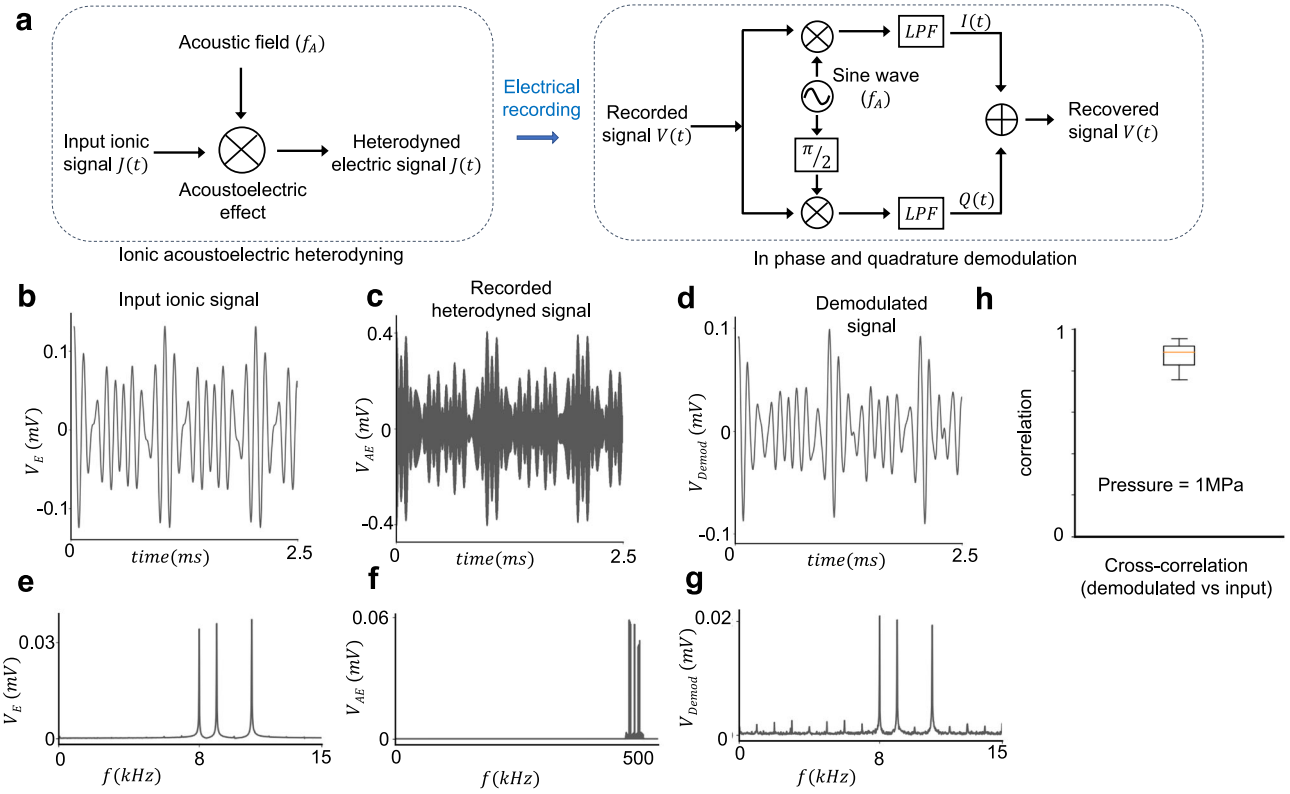


Fig. 5 Acoustoelectric ion current heterodyning in a tissue phantom. a Schematic of the acoustoelectric heterodyning and demodulation procedure. An ionic current signal in the target location is focally mixed with a sinusoidal acoustic signal via the acoustoelectric effect to generate an electric signal with the original information but now modulated up to the acoustic frequency f_A. The electric potential of the modulated signal is recorded and computationally demodulated to recover the original signal via in-phase and quadrature (IQ) demodulation. In IQ demodulation, the signal is multiplied by two sinusoidal waveforms at the known frequency f_A and a $\pi/2$ phase difference. The resultant signals are low pass filtered (LPF) to yield the $I(t)$ signal and the $Q(t)$ phase-shifted signal from which the instantaneous amplitude and phase of the demodulated signal are recovered. **b**–**g** Representative traces of the ionic acoustoelectric heterodyning and demodulation, shown are **b** input ionic signal, **c** recorded potential of the acoustically heterodyned electric signal, high-passed filtered in software to remove the applied ionic signal, **d** computationally demodulated signal, **e** amplitude spectrum density (ASD) of the signal in (**b**), **f** ASD of the signal in (**c**), **g** ASD of the signal in (**d**), the small extra peaks are caused by intermodulation—where the sum and difference frequencies interfere with the original applied fields[49]. **h** Cross-correlation between the demodulated signal and the input signal; $n = 10$ measurements.

performed by solving Eq. (8) for the induced electric potential ϕ_{ae}, with $\vec{E}_{ae} = -\nabla\phi_{ae}$. The result is obtained by solving the Poisson equation $\Delta \cdot (\phi_{ae}) = \nabla(\beta P) \cdot (\vec{E}_0)$ with a source term $S = -\nabla(\beta P) \cdot (\vec{E}_0)$, using a custom Python script. To compute the source term, the applied acoustic field P was computed with an analytic solution for an ideal focused spherical ultrasound transducer using a summation of Bessel functions[31]. The applied electric field $\vec{E}_0$ was assumed to be homogenous (constant orientation and magnitude). The dot product of ∇P and $\vec{E}_0$ was computed and then multiplied by the constant k (i.e. $1e^{-9}$ Pa^{-1})[27,28]. To solve the Laplacian in the Poisson equation for the electric potential ϕ_{ae}, we implemented a Fast-Poisson-Solver[50] (since σ was homogeneous), leading to a diagonal system in Fourier-space (k-space). The Fourier transformation of the source term S resulted in $k^2\widehat{\phi_{ae}}(k) = -\hat{S}(k)$, where $\hat{f}(k)$ denotes the spatial Fourier transformation of $f(x)$. Then $\widehat{\phi_{ae}}(k) = -\hat{S}(k)/(k^2)$ and ϕ_{ae} were obtained through an inverse Fourier transformation. $\vec{E}_{ae}$ was obtained as the negative gradient of ϕ_{ae} or by multiplying with $-i\vec{k}$ before inverting the transformation component-wise.

Measurements of the acoustoelectric fields

Phantom. The measurements of the acoustoelectric modulation of the applied electric fields were done in a custom-built acrylic tank (50 cm × 20 cm × 20 cm) divided into two parts with a 12 µm thick acoustically transparent Polyvinylidene difluoride (PVDF) film. In one part of the tank, the ultrasound transducer was mounted and immersed in nonconductive mineral oil to minimize electromagnetic interference from the transducer to the recording area. In the second part of the tank, the stimulation electrodes, recording electrodes, and hydrophone were placed and immersed in 0.9% saline. An acoustic damping material (Aptflex-36) was attached to the back of the tank to minimize acoustic reflections. The phantom tank was covered with a Faraday cage to reduce electromagnetic interference. See Supplementary Fig. 5a, b for a diagram of the instrumentation photo of experimental set up.

Probe scanning. The stimulation electrode-pair, recording electrode, and recording hydrophone were mounted using a 3D printed adapter on an XYZ stage[51] (Q5 Delta 3D Printer, FLSUN) and scanned across the ultrasonic focal area in 0.5 mm increments. The scanning was controlled via G-Code commands sent through a custom Python 3 interface.

Data acquisition. All applied and monitored signals were at 5MS/s, and all applied and monitored signals were time synced using a CMI interface between the function generators and oscilloscopes with trigger inputs. The applied voltages, monitor channels and electric potentials were logged using data acquisition hardware (WiFiScope WS5, TiePie engineering, Netherlands, WiFiScope WS6 DIFF). The logged signals were streamed from the data acquisition hardware to a workstation PC using custom C code which utilized the Tiepie SDK to control the triggers, channels, and function generator output. The compiled C code which called the oscilloscope commands was in turn called within a Python wrapper, which also sent G-code commands to the *XYZ* stage and controlled a relay to turn off all equipment in the Faraday cage during recording, including the motor of the stage which we found emitted low-level electromagnetic interference. In each measurement, the pressure focus was first automatically found using a custom script that searched for the peak pressure first in the radial planes and then along the axial axis.

Acoustic fields application. The acoustic field was applied using a curved ceramic (PZT) 500 kHz ultrasound transducer (60 mm diameter, 63.5 mm acoustic path length; Precision Acoustics Ltd, UK). The ultrasound transducer was driven by an arbitrary function generator (Handyscope HS5, TiePie engineering, Netherlands) and a 40 W linear power amplifier (240 L, Electronics & Innovation Ltd).

Electric fields application. The electric field was applied using a pair of 98% platinum iridium wire electrodes (0.25 mm cross-section diameter, 1.4 mm length exposed tips; Alfa Aesar) with 3 mm inter-electrode spacing. The electrodes were

driven by a second arbitrary function generator (Handyscope HS5, TiePie engineering, Netherlands) and a custom-made high-frequency voltage source made of glass core transformers (Hitachi Metals) with a maximum ±20 V amplitude at an effective 3 dB bandwidth range of 5 kHz to 2 MHz. In a subset of measurements in which frequencies lower than 5 kHz were applied, the electrodes were driven directly from the arbitrary function generator.

Pressure recordings. The acoustic field was measured using a 0.2 mm needle hydrophone (52 mV/kPa at 500 kHz calibration; Precision Acoustics Ltd) and a DC-coupled preamplifier (Precision Acoustics Ltd).

Electric potential recordings. The electric potentials were measured through a recording electrode similar to the stimulation electrodes, which was placed between the two stimulation electrodes. The recorded potential was amplified using a low-noise differential amplifier (SR560, Stanford Research Systems) and filtered using a custom-built[52,53] passive differential high or low-pass filter to filter out the signal at the frequency of the applied electric field while allowing the sum and difference frequencies to reach the amplifier unattenuated.

The specific settings of each measurement were:

Figure 3d–f: The reference electrode position was at the back of the phantom next to the acoustic damping material in the corner, and the gain on the SR560 preamp was 500. A 100 kHz analogue high pass filter with the design shown in Supplementary Fig. 5c was placed before the signal reached the preamp.

Figure 3g–i: The electrodes were arranged as shown in Fig. 3b, c, but the analogue filter before the preamp was exchanged for a low pass filter (5 kHz cut-off frequency) such that the high frequency (499.99 kHz) electric field is removed before the remaining signal enters the preamplifier. The design for the differential low-pass filter is also shown in Supplementary Fig. 5d.

Figure 4a, b: For the spatial 2D maps, electrodes were placed as in Fig. 3. For the 2-dimensional mapping, a recording was made for each pixel. For each recording, the electric field was ramped at the beginning and end to avoid voltage spike transients in the preamplifier. The previously described high pass filter was used as an 8 kHz applied electric field was applied. A half-amplitude, two-wavelength duration acoustic signal was applied at the beginning of each recording, and that marker was used to time synchronize the measurement data. After applying digital filtering to isolate the sum and difference frequencies in the recorded electric signals, they were combined into a single three-dimensional array (one time and two spatial dimensions). The reconstructed $\phi_{ae}(t)$ was used to visualize the time evolution ($\hat{x}\hat{y}$ and $\hat{x}\hat{z}$ views). A viewing tool is provided along with the code and data in the online repository to scroll through the reconstructed transient $\hat{x}\hat{y}$ and $\hat{x}\hat{z}$ views.

Figure 4c, d: All parameters were the same as in Fig. 4a-b, and all electrodes were located as in Fig. 3, except for the reference location, which was moved closer and into the null area shown in the simulation prediction. This produced a clearer spatial map, potentially due to minimized edge diffraction/reflection interferences with the smaller amplitude acoustoelectric signals.

Figure 4f, g: Same as in Fig. 4a, b.

Fig. 5: For the IQ demodulation, a hardware high-pass filter (third-order differential Butterworth 100 kHz cut-off) was applied as before to ensure we completely removed the original low-frequency signal so that it doesn't enter the preamp so that we can apply a gain of 500 without saturating. We performed IQ demodulation on this recorded signal. This hardware filter innately introduced a time lag between the complex ionic input signal and the recorded signal, which we overcame through the use of rolling cross-correlation to find the optimal phase offset, as well as the maximal point of correlation using Pearson's correlation coefficient[54,55], as it is not amplitude dependent when using normalized inputs. This coefficient was reported over a range of recordings with mean and standard deviation.

Supplementary Fig. 4c: To obtain a frequency sweep, no analogue filters could be used, as this would affect the amplitude of the results. This also means that the preamplifier cannot be used as the applied electric field would saturate the preamplifier obscuring the acoustoelectrically generated sum and difference frequencies. Therefore, the measurements were made without amplification, which was possible due to the continuous, single frequency characteristic of the applied signals that yield high SNR sum and difference frequencies over an 8 s period. The electrodes were arranged as shown in Fig. 3b.

Noise and artefacts. To reduce noise and electromagnetic artefacts, the measurement area was enclosed by a custom-built Faraday cage made from 3 mm spaced copper mesh. In addition, a relay was used to turn off the 3D printer motor (the only other electrically powered device within the Faraday Cage) while recording. A set of tests detailed in Supplementary Figure 4 were designed to show the acoustoelectric measurement made was not an artefact due to conductive connection with the RF amplifier, electrode vibration, or application of the acoustic or electric fields alone. Previous acoustoelectric studies cite noise[56] as being a major issue. However, these studies measured a single acoustoelectric pulse signal of a few acoustic periods duration, which results in a broader, more complex spectrum in Fourier space. Since we applied continuous, single-frequency exposure for much longer (8 s) intervals, the signal-to-noise ratio was vastly improved. Furthermore, since the interaction was a multiplication of simple sine waves instead of a multiplication of commonly employed square pulse waves the resulting field only consists of the sum and difference frequencies of the applied fields, rather than the broad-spectrum characteristic of square-shaped pulses. We did find noise due to the presence of strong electric field exposure, which is unchanged when an acoustic field is also applied. This is likely due to Faradaic electrochemical reactions[57] taking place at the electrode/liquid interface and appearing as a DC offset increasing in time (see Supplementary Figure 4e).

Signal processing and analysis. Custom Python 3.8.4 scripts were created to create the data analysis toolchains using Numpy, Scipy, OpenCV2 and Pandas libraries.

Time domain analysis. To isolate the heterodyned high-frequency acoustoelectric signal, in the case of an applied 8 kHz electric field and 500 kHz acoustic field, a 17th-order Chebyshev II digital bandpass filter was applied from 100 Hz below the difference frequency, up to 100 Hz above the sum frequency. A similar filter strategy was applied when the applied electric field was at different frequencies, whereby the pass band started 100 Hz below the difference frequency and stopped 100 Hz above the sum frequency.

Frequency domain analysis. A 1-D discrete Fourier Transform[58] with Flat Top[59,60] window to optimize amplitude accuracy was computed, as we report amplitude spectral density (ASD) instead of power spectral density (PSD) to easily read the average peak-to-peak amplitude of each measurement. After the Fourier transform is computed, the two-sided amplitude spectrum was multiplied by 2, and half the array was taken—converting it into its single-sided form. The units of the single-sided amplitude spectrum then give the mean peak amplitude of each sinusoidal component making up the time-domain signal.

2D field image reconstruction. After the filtered acoustoelectric data was compiled into a large three-dimensional array (X,Y, time), we applied a 2D low-pass image filter with a Gaussian Convolution kernel of 5 pixels to smooth the resulting images. Since the pixel resolution was limited by the 0.5 mm increment resolution of the delta printer we used for scanning, the averaging filter (particularly in the XZ compiled data) would bias the minima and maxima to zero as it averaged over the periodic dipole (500 kHz ultrasound wavelength ≈ 3 mm, of similar width to the convolution kernel), so that we then rescaled the filtered image by the minima and maxima range of the unfiltered image to obtain an accurate representation of amplitude, whilst also denoising the resultant 2D measurement image.

IQ demodulation. IQ demodulation was carried out on a heterodyned recorded signal ($8 + 9 + 11$ kHz sine wave). To demodulate the recorded signal, we multiply it by a simulated 500 kHz sine wave carrier, and a 90° phase offset signal. We add these together to return a demodulated signal. To ensure we reduce spurious harmonics[61] we then low-pass filter the result using a 17th-order Chebyshev II digital lowpass filter with 20 kHz cut-off frequency.

Statistical tests. All data is shown as mean ± SD. Statistical tests are specified in respective tables and figure legends. Statistical significance was tested using paired t-test and Tukey's honest significance test[62] corrected for multiple comparisons.

Data availability

Data supporting the findings are available at https://doi.org/10.6084/m9.figshare.c.6365098. Further information is available from the corresponding author upon request.

Code availability

Analysis tools and code supporting the findings are available at https://doi.org/10.6084/m9.figshare.c.6365098. Further information is available from the corresponding author upon request. The code is also available on github at: https://github.com/Acoustoelectric/Acoustoelectric.git

Received: 16 September 2022; Accepted: 6 April 2023;
Published online: 20 April 2023

References

1. Weik, M. H. *Computer Science and Communications Dictionary*. 720–720 (Springer, 2000).
2. Bardeen, J. & Brattain, W. H. The transistor, a semi-conductor triode. *Phys. Rev.* **74**, 230–231 (1948).
3. Goldsmith, A. *Wireless Communications*. 1–644 (Cambridge University Press, 2005).

4. Protopopov, V. V. Principles of optical heterodyning. *Springer Ser. Opt. Sci.* **149**, 1–49 (2010).
5. Tikan, A., Bielawski, S., Szwaj, C., Randoux, S. & Suret, P. Single-shot measurement of phase and amplitude by using a heterodyne time-lens system and ultrafast digital time-holography. *Nat. Photonics* **12**, 228–234 (2018).
6. Mumma, M., Kostiuk, T., Cohen, S., Buhl, D. & Von Thuna, P. C. Infrared heterodyne spectroscopy of astronomical and laboratory sources at 8.5 μm. *Nature* **253**, 514–516 (1975).
7. Glover, T. E. et al. X-ray and optical wave mixing. *Nature* **488**, 603–608 (2012).
8. Schmitt, S. et al. Submillihertz magnetic spectroscopy performed with a nanoscale quantum sensor. *Science (1979)* **356**, 832–837 (2017).
9. Stremler, F. G. *Introduction to Communication Systems* 3rd edn, 195–197 (Addison-Wesley Publishing Co., 1990).
10. Kousseff, C. J., Halaksa, R., Parr, Z. S. & Nielsen, C. B. Mixed ionic and electronic conduction in small-molecule semiconductors. *Chemical Reviews* **122**, 4397–4419 (2021).
11. Nawaz, A., Liu, Q., Leong, W. L., Fairfull-Smith, K. E. & Sonar, P. Organic electrochemical transistors for in vivo bioelectronics. *Adv. Mater.* **33**, 2101874 (2021).
12. Ohayon, D. & Inal, S. Organic bioelectronics: from functional materials to next-generation devices and power sources. *Adv. Mater.* **32**, 2001439 (2020).
13. Steinmetz, C. P. *Theory and Calculation of Transient Electric Phenomena and Oscillations*, 1865–1923 (Kessinger Publishing, LLC, 1920).
14. Thomenius, K. E. Evolution of ultrasound beamformers. In Proc. *IEEE Ultrason. Symp.* Vol. 2, 1615–1622 (1996).
15. Richards, L. A., Cleveland, R. & Stride, E. P. Creating uniform ultrasound fields in the brain without an array. *J. Acoust. Soc. Am.* **144**, 1699 (2018).
16. Tichý, J. et al. *Fundamentals of Piezoelectric Sensorics: Mechanical, Dielectric, and Thermodynamical Properties of Piezoelectric Materials*. (Springer-Verlag, Heidelberg, 2010).
17. Fox, F. E., Herzfeld, K. F. & Rock, G. D. The effect of ultrasonic waves on the conductivity of salt solutions. *Phys. Rev.* **70**, 329–339 (1946).
18. Surya Santoso, Ph. D. & Beaty, H. W. *Standard Handbook for Electrical Engineers* 17th edn, (McGraw-Hill Education, 2018).
19. Yang, R., Li, X., Liu, J. & He, B. 3D current source density imaging based on the acoustoelectric effect: a simulation study using unipolar pulses. *Phys. Med. Biol.* **56**, 3825–3842 (2011).
20. Olafsson, R. et al. Ultrasound current source density imaging. *IEEE Trans. Biomed. Eng.* **55**, 1840–1848 (2008).
21. Yang, R., Li, X., Song, A., He, B. & Yan, R. A 3-D reconstruction solution to current density imaging based on acoustoelectric effect by deconvolution: a simulation study. *IEEE Trans. Biomed. Eng.* **60**, 1181–1190 (2013).
22. Berthon, B., Dansette, P. M., Tanter, M., Pernot, M. & Provost, J. An integrated and highly sensitive ultrafast acoustoelectric imaging system for biomedical applications. *Phys. Med. Biol.* **62**, 5808–5822 (2017).
23. Lavandier, B., Jossinet, J. & Cathignol, D. Experimental measurement of the acousto-electric interaction signal in saline solution. *Ultrasonics* **38**, 929–936 (2000).
24. Lavandier, B., Jossinet, J. & Cathignol, D. Quantitative assessment of ultrasound-induced resistance change in saline solution. *Med. Biol. Eng. Comput* **38**, 150–155 (2000).
25. Olafsson, R., Witte, R. S. & O'Donnell, M. Measurement of a 2D electric dipole field using the acousto-electric effect. *Proc. SPIE 6513, Medical Imaging 2007: Ultrasonic Imaging and Signal Processing*, 65130S (2007).
26. Grant, I. S. & Phillips, W. R. *Electromagnetism* 2nd edn, 122–123 (Wiley, 1991).
27. Jossinet, J., Lavandier, B. & Cathignol, D. Impedance modulation by pulsed ultrasound. *Ann. N. Y. Acad. Sci.* **873**, 396–407 (1999).
28. Song, X., Qin, Y., Xu, Y., Ingram, P. & Witte, R. S. Tissue acoustoelectric effect modeling from solid mechanics theory. *IEEE Trans. Ultrason. Ferroelectr. Freq. Control* **64**, 1583–1590 (2017).
29. Chen, P. et al. Acoustic characterization of tissue-mimicking materials for ultrasound perfusion imaging research. *Ultrasound Med. Biol.* **48**, 124–142 (2022).
30. McGarry, C. K. et al. Tissue mimicking materials for imaging and therapy phantoms: a review. *Phys. Med. Biol.* **65** 23TR01 (2020).
31. Parker, K. J. Radiation pattern of a focused transducer: a numerically convergent solution. *J. Acoust. Soc. Am.* **94**, 2979–2991 (1993).
32. Li, Q., Olafsson, R., Ingram, P., Wang, Z. & Witte, R. Measuring the acoustoelectric interaction constant using ultrasound current source density imaging. *Phys. Med. Biol.* **57**, 5929–5941 (2012).
33. Gabriel, C. Compilation of the dielectric properties of body tissues at RF and microwave frequencies. (King's College London, 1996).
34. Ward, L. M. Synchronous neural oscillations and cognitive processes. *Trends Cogn. Sci.* **7**, 553–559 (2003).
35. Grossman, N. et al. Noninvasive deep brain stimulation via temporally interfering electric fields. *Cell* **169**, 1029–1041.e16 (2017).
36. Hutcheon, B. & Yarom, Y. Resonance, oscillation and the intrinsic frequency preferences of neurons. *Trends Neurosci.* **23**, 216–222 (2000).
37. Heddle, D. W. O. *Electrostatic Lens Systems*. 59 (CRC Press, 2000).
38. Blewett, J. P. Radial focusing in the linear accelerator. *Phys. Rev.* **88**, 1197–1199 (1952).
39. Fine, R. A. & Millero, F. J. Compressibility of water as a function of temperature and pressure. *J. Chem. Phys.* **59**, 5529 (2003).
40. Sacko, D. & Kéïta, A. A. Techniques of modulation: pulse amplitude modulation, pulse width modulation, pulse position modulation. *Int. J. Eng. Adv. Technol.* **7**, 2249–8958 (2017).
41. Räisänen, A. V. & Lehto, A. *Radio Engineering for Wireless Communication and Sensor Applications*, (Artech House, 2003).
42. Stanford Research Systems, *Lock-In Amplifier Basics Application Note*, (Stanford Research Systems Inc, SunnyVale, 2020).
43. Blaunstein, N., Christodoulou, C. & Sergeev, M. *Introduction to Radio Engineering*. (CRC Press, 2016).
44. Courant, E. D. & Snyder, H. S. Theory of the alternating-gradient synchrotron. *Ann. Phys. (N. Y)* **3**, 360–408 (1958).
45. Brain, M. E. R., Hutcheon, B. & Yarom, Y. Resonance, oscillation and the intrinsic frequency preferences of neurons. *Trends Neurosci.* **23**, 216–222 (2000).
46. Ozen, S. et al. Transcranial electric stimulation entrains cortical neuronal populations in rats. *J. Neurosci.* **30**, 11476–11485 (2010).
47. Rattay, F. The basic mechanism for the electrical stimulation of the nervous system. *Neuroscience* **89**, 335–346 (1999).
48. Berkelmann, L. et al. Tumour-treating fields (TTFields): Investigations on the mechanism of action by electromagnetic exposure of cells in telophase/cytokinesis. *Sci. Rep.* **9**, 1–11 (2019).
49. Babcock, W. C. Intermodulation interference in radio systems: frequency of occurrence and control by channel selection. *Bell Syst. Tech. J.* **32**, 63–73 (1953).
50. Langlands, T. A. M. & Henry, B. I. The accuracy and stability of an implicit solution method for the fractional diffusion equation. *J. Comput. Phys.* **205**, 719–736 (2005).
51. Xu, K., Kim, Y., Boctor, E. M. & Zhang, H. K. Enabling low-cost point-of-care ultrasound imaging system using single element transducer and delta configuration actuator. **31**, (Conference of Medical Imaging, San Diego, 2019).
52. Chan, K. Application Report Design of Differential Filters for High-Speed Signal Chains (Texas Instruments, 2007).
53. Casas, Ó. & Pallás-Areny, R. Basics of analog differential filters. *IEEE Trans. Instrum. Meas.* **45**, 275–279 (1996).
54. Weisstein, Eric W. "Correlation Coefficient." From MathWorld--A Wolfram Web Resource. https://mathworld.wolfram.com/CorrelationCoefficient.html.
55. Hotelling, H. New light on the correlation coefficient and its transforms. *J. R. Stat. Soc. Ser. B (Methodol.)* **15**, 193–225 (1953).
56. Tseng, H. W., Qin, Y., O'Donnell, M., Witte, R. S. Improving sensitivity in acoustoelectric imaging with coded excitation and optimized inverse filter. (IEEE International Ultrasonics Symposium, IUS, 2017).
57. Biesheuvel, P. M., Porada, S. & Dykstra, J. E. The difference between Faradaic and non-Faradaic electrode processes. *arXiv:*1809.02930 (2018).
58. Cooley, J. W. & Tukey, J. W. An Algorithm for the Machine Calculation of Complex Fourier Series. *Mathematics and Computation* Vol. 19, 297–01 (1965).
59. F. J. Harris, On the use of windows for harmonic analysis with the discrete Fourier transform, *Proceedings of the IEEE*, vol. 66, 51–83 (1978).
60. Heinzel, G., Rüdiger, A. & Schilling, R. Spectrum and spectral density estimation by the Discrete Fourier transform (DFT), including a comprehensive list of window functions and some new flat-top windows. *Technical Report* (Albert-Einstein-Institut, Hannover, 2002).
61. Dayan, A., Huang, Y. & Schuchinsky, A. Passive intermodulation at contacts of rough conductors. *Electron. Mater.* **3**, 65–81 (2022).
62. Tukey, J. W. Comparing individual means in the analysis of variance. *Biometrics* **5**, 99 (1949).

Acknowledgements

We thank David Bono and Xinghao Cheng for assisting with the experimental setup. N.G. was funded by the UK Dementia Research Institute (UK DRI)—an initiative funded by the Medical Research Council, Engineering and Physical Sciences Research Council (EPSRC) UK, Science & PINS Award for Neuromodulation, and NIHR IBRC Confident in Concept Award.

Author contributions

J.L.R. designed and developed the hardware, simulations and experiments and wrote the paper. E.N. devised the equation for the acoustoelectric effect and revised the paper. C.B. revised the paper. R.C. provided the analytic solution code for a focused spherical transducer and revised the paper. N.G. designed experiments, wrote the paper, and oversaw experiments.

Competing interests

J.L.R. and N.G. have applied for a patent on the technology, assigned to Imperial College London. The rest of the authors declare no competing interests.

Additional information

Supplementary information The online version contains supplementary material available at https://doi.org/10.1038/s42005-023-01198-w.

Correspondence and requests for materials should be addressed to Nir Grossman.

Peer review information *Communications Physics* thanks Jonas Meinel and the other, anonymous, reviewer(s) for their contribution to the peer review of this work. Peer reviewer reports are available.

Reprints and permission information is available at http://www.nature.com/reprints

Publisher's note Springer Nature remains neutral with regard to jurisdictional claims in published maps and institutional affiliations.

Open Access This article is licensed under a Creative Commons Attribution 4.0 International License, which permits use, sharing, adaptation, distribution and reproduction in any medium or format, as long as you give appropriate credit to the original author(s) and the source, provide a link to the Creative Commons license, and indicate if changes were made. The images or other third party material in this article are included in the article's Creative Commons license, unless indicated otherwise in a credit line to the material. If material is not included in the article's Creative Commons license and your intended use is not permitted by statutory regulation or exceeds the permitted use, you will need to obtain permission directly from the copyright holder. To view a copy of this license, visit http://creativecommons.org/licenses/by/4.0/.

© The Author(s) 2023